INTERNATIONAL JOURNAL FOR NUMERICAL METHOD IN FLUIDS, VOL.20, 1315–1336 (1995)

AN EFFICIENT NUMERICAL TANK FOR NON-LINEAR WATER WAVES, BASED ON THE MULTI-SUBDOMAIN APPROACH WITH BEM

PEI WANG, YITAO YAO AND MARSHALL P. TULIN

Ocean Engineering Laboratory, University of California, Santa Barbara, CA 93106-0001, U.S.A.

SUMMARY

An efficient 2D non-linear numerical wave tank called *LONGTANK* has been developed based on a multi-subdomain (MSD) approach combined with the conventional boundary element method (BEM). The multi-subdomain approach aims at optimized matrix diagonalization, thus minimizing the computing time and reserved storage. The CPU per time step in *LONGTANK* simulations is found to increase only linearly with the number of surface nodes, which makes *LONGTANK* highly efficient especially when simulating long-time wave evolutions in space.

Appropriate treatment of special points on the boundary ensures high resolution in *LONGTANK* simulation beyond initial deformation and breaking, which allows detailed study of breaking criterion, breaker morphology, breaking dissipation, vorticity generation, etc.

Detailed numerical implementation has been given with demonstration of *LONGTANK* simulations.

KEY WORDS: numerical wave tank; multi-subdomain approach; non-linear water waves; wave breaking

1. INTRODUCTION

In connection with energetic waves on the ocean, there is now great interest in planar wave groups and in wave deformation and breaking within such groups.[1] The non-linear processes at work, leading to breakdown, are largely not susceptible to purely theoretical analysis. For understanding of these processes, numerical simulation is required.

The numerical simulation of non-linear progressive, surface waves in one dimension was earlier carried out by Dold and Peregrine[2] and Vinje and Brevig,[3] making use of boundary elements and of the method of wave projection in time due to Longuet-Higgins and Cokelet.[4] This early work took the wave trains to be periodic and was limited to a small number of waves. Utilizing iterating matrix solutions, Dold and Peregrine[2] found the computing time to increase as the square of the number of surface nodes; this fact limited these boundary element computations to $x/\lambda = O(10)$, where λ is the wavelength and x is the tank length.

The numerical simulation of tank wavemaking was carried out by Lin *et al.*[5] and subsequently by Dommermuth *et al*,[6] Grilli *et al.*[7] and Cointe,[8] again for a small number of waves, $O(10)$.

The numerical modelling of water-wave-connected problems, especially in a wave tank, is always composed of three elements:[7] wave generation, propagation and absorption. The efficiency of a numerical wave tank depends not only on the quality of the wave absorption technique, which allows

CCC 0271–2091/95/121315–22

Received 24 November 1993
Revised 22 September 1994

the tank length to be most effectively used, but also on the computational method for the calculation of wave propagation for large distances, which is crucial for the simulation of non-linear processes in real wave trains under unstable conditions. Experiments of Su and Green[9] show that the downtank distance necessary for non-linear wave processes to produce strong spatial variations leading to breaking increases with decreasing initial wave steepness a_0k_0, roughly as $(a_0k_0)^{-2}$, and $x/\lambda = O(100)$ is required for $a_0k_0 = O(10^{-1})$. This is a distance roughly one order of magnitude larger than numerical tank lengths achieved prior to the present work.

We have developed a two-dimensional numerical wave tank called *LONGTANK*; a tank length (x/λ) of 110 has been achieved utilizing a multi-subdomain approach together with the boundary element method. In our application the size of subdomains has been optimized for computational efficiency. The present approach features matrix block-diagonalization and has both the advantages of the boundary element method, which reduces the dimension of the problem, and of space discretization methods, which limits the bandwidth in the system matrix. *LONGTANK* is thus highly efficient for wave calculations, allowing non-linear wave evolution to sufficiently long distances, while the CPU in each step increases only linearly with the number of surface nodes. The latter is evidence of the success of this computational method.

The efficiency of *LONGTANK* is further enhanced by installation of a moving beach before the front of the entire wave train to absorb longer weak waves that leak through the front but are of no interest for the study of non-linear wave phenomena. The damping technique used by Baker *et al.*[10] and more recently by Cointe,[8] which has been demonstrated to be efficient for attenuating monochromic waves, is extended here to damp more general waves.

The methodology of *LONGTANK* is presented in the following sections with examples of *LONGTANK* simulations. Basic formulations of the free surface flow and the boundary integral equation utilizing the method of Green functions are given in Section 2. The multi-subdomain approach, which contributes to the high efficiency of *LONGTANK*, is presented in Section 3. The numerical procedures of *LONGTANK*, including tank set-up, boundary discretization and integration, treatment at special points on the boundaries, the moving beach and jet impact conditions, etc., are discussed in Section 4. Some *LONGTANK* simulations of wave evolution, deformation and breaking are demonstrated and compared with experiments to show the powerful capability of *LONGTANK* and to validate its high accuracy. Some of the results have been presented and discussed in previous papers[11–13] which emphasized physical applications of *LONGTANK*.

2. THEORETICAL FORMULATIONS

Longuet-Higgins and Cokelet[4] pioneered the numerical computation of non-linear surface gravity waves in deep water by following the time history of space-periodic irrotational surface waves, represented by the independent co-ordinates and the velocity potential of marked particles at the free surface, and solving an integral equation at each time step for new normal velocities.

This method has been followed by others and extended to study comprehensive non-linear surface wave problems and has divided into two main branches: formulating two-dimensional problems in the complex plane by defining a streamfunction ψ[2,3,6,14] and using potential theory and a Green function.[7,8] Both approaches are appropriate to solve two-dimensional surface wave motions, but the latter has the potential to deal with three-dimensional problems and thus is chosen here.

We assume that the fluid is inviscid and incompressible and the flow is irrotational. The effects of surface tension can be included, but they are ignored in most cases we have studied.

Consider a volume of water, Ω, surrounded by boundaries consisting of the water surface Γ_S, tank bottom Γ_B, and side walls Γ_W, and let (x, y, z) denote rectangular co-ordinates with the x- and y-axes lying on the mean surface and the z-axis vertical and upward.

With the approximation of incompressibility and irrotationality, the fluid velocity $\vec{u}$ becomes the gradient of the velocity potential ϕ and Laplace's equation is satisfied everywhere in the volume Ω:

$$\vec{u} = \nabla\phi, \tag{1}$$

$$\nabla \cdot \vec{u} = \nabla^2\phi = 0. \tag{2}$$

Thus the velocity potential and velocity field within Ω are uniquely determined by their values on the boundaries Γ_S, Γ_B, and Γ_W and can be solved by the Green function method.

At the free surface $\eta = \eta(x, y, t)$ we have the kinematic conditions

$$\frac{Dx}{Dt} = \frac{\partial\phi}{\partial x}, \qquad \frac{Dy}{Dt} = \frac{\partial\phi}{\partial y}, \tag{3}$$

where $D/Dt = \partial/\partial t + \nabla\phi \cdot \nabla$ denotes the material derivative or differentiation following a given particle.

The rate of change in potential ϕ can be immediately derived from Bernoulli's equation:

$$\frac{D\phi}{Dt} = -\frac{p - p_a}{\rho} - gy + \tfrac{1}{2}(\nabla\phi)^2, \tag{4}$$

where p_a is the atmospheric pressure.

The pressure on the surface, p, is normally equal to atmospheric pressure in the absence of surface tension. With surface tension T_s, we have

$$p - p_a = -T_s(\nabla \cdot \vec{n}). \tag{5}$$

The boundary integral equation for the solution of the normal derivative of the potential at the water surface is formulated by applying Green's theorem, which states

$$\alpha\phi(P) = \int_\Gamma \left(\phi \frac{\partial}{\partial n}(\ln r) - \ln r \frac{\partial\phi}{\partial n}\right) d\Gamma, \tag{6}$$

where α is the interior angle at the field point P lying on the boundary and $\alpha = 2\pi$ when P is inside Ω.

For the time domain calculation of the surface wave motion in a wave tank, mixed boundary conditions may be imposed. On the water surface Γ_s the velocity potential is known from previous time steps and the normal derivative of the potential is the unknown variable; on the boundary of the wavemaker, Γ_{WM}, the normal velocity of the water particle is known to be equal to the normal velocity of the wavemaker; on the tank bottom Γ_B and the end wall of the tank Γ_{EW}, the normal velocity is zero. Thus equation (6) is applied in two different forms on different parts of the boundary.

$P \in \Gamma_s$ *(boundary with Dirichlet condition)*

$$\begin{aligned}\int_{\Gamma_{WM}\cap\Gamma_B\cap\Gamma_{EW}} \phi(Q)\frac{\partial}{\partial n}\ln r(P, Q)\, d\Gamma - \int_{\Gamma_S} \frac{\partial\phi}{\partial n}(Q)\ln r(P, Q)\, d\Gamma \\ = -\alpha(P)\phi(P) + \int_{\Gamma_S} \phi(Q)\frac{\partial}{\partial n}\ln r(P, Q)\, d\Gamma \\ - \int_{\Gamma_{WM}\cap\Gamma_B\cap\Gamma_{EW}} \frac{\partial\phi}{\partial n}(Q)\ln r(P, Q)\, d\Gamma.\end{aligned} \tag{7a}$$

$P \in \Gamma_{WM} \cap \Gamma_B \cap \Gamma_{EW}$ *(boundary with Neumann condition)*

$$\alpha(P)\phi(P) + \int_{\Gamma_{WM}\cap\Gamma_B\cap\Gamma_{EW}} \phi(Q)\frac{\partial}{\partial n} \ln r(P, Q)\, d\Gamma - \int_{\Gamma_S} \frac{\partial\phi}{\partial n}(Q) \ln r(P, Q)\, d\Gamma$$
$$= \int_{\Gamma_S} \phi(Q)\frac{\partial}{\partial n} \ln r(P, Q)\, d\Gamma - \int_{\Gamma_{WM}\cap\Gamma_B\cap\Gamma_{EW}} \frac{\partial\phi}{\partial n}(Q) \ln r(P, Q)\, d\Gamma. \quad (7b)$$

3. MULTI-SUBDOMAIN APPROACH

The numerical treatment of problems in potential theory by the boundary element method is classical. A distinct advantage of the boundary element method over the finite difference and finite element methods is that the space dimension of the problem is reduced by one. However, this is accompanied by the disadvantage of a full system matrix established along the whole boundary; the time to generate such a full matrix and to solve the corresponding algebraic equations requires about a cubic increase in computing time with the number of nodes on the entire boundary. Yueng[15] discussed the relative efficiency among various numerical methods and gave a formula for comparison which shows that for surface flow problems with a large computational domain both the boundary element method and space discretization methods are inefficient and costly.

The multi-subdomain approach used in *LONGTANK* (see Figure 1) takes advantage of both boundary element and space discretization methods: the fluid domain is divided into a set of subdomains (or super elements) and the BEM formulation is applied to each subdomain. Therefore the coefficient matrix of the simultaneous equations becomes block-banded. With optimization the total number of influence coefficients from the BEM formulation will be significantly reduced and the computing time for solving the algebraic equations will also be significantly reduced utilizing the banded solver.

To study strong wave modulation leading to wave breaking in an unstable wave system of small initial steepness, the tank has to be long enough. Therefore the computational domain is rectangular with a much larger number of grid points on the free surface than on the two ends. This is ideal for introducing the multi-subdomain approach, which is especially aimed at optimized 'matrix diagonalization'.

3.1. Matrix block diagonalization

By inserting vertical numerical inner boundaries in the tank with no physical significance, the whole computational domain is divided into a set of parallel subdomains (see Figure 2(a)). On these common boundaries both the potential and its normal derivatives are unknown *a priori*. Two equations can be established at each point on these boundaries, since the BEM formulation will apply to subdomains on either side. In each subdomain a set of linear algebraic equations is formed with the coefficients only

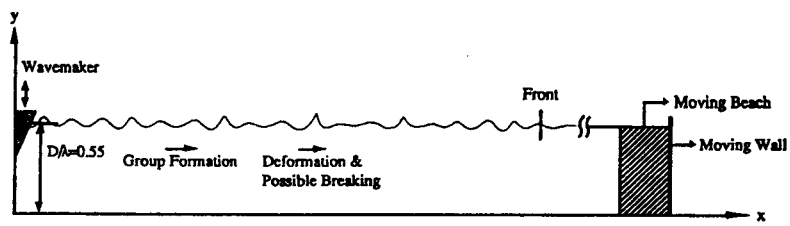

Figure 1. Schematic of non-linear numerical wave tank, LONGTANK

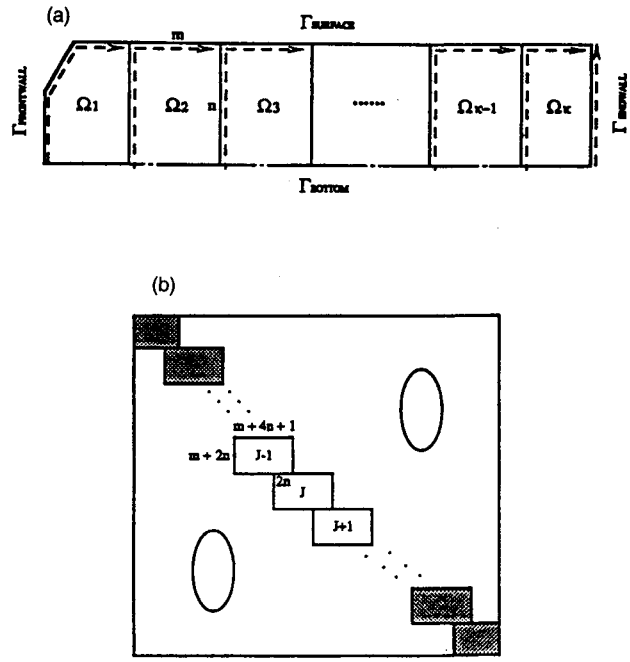

Figure 2. Implementation of multi-subdomain approach (a) Computational domain divided into subdomains (schematic). Dashed lines with arrows indicate the sequence of global numbering when the boundaries are discretized; m, the number of panels on the surface in one subdomain; n, the number of panels on vertical walls. The dotted line implies an image being introduced to exclude the bottom boundary. (b) Showing the diagonalized coefficient matrix

involving grid points on the boundaries of the same subdomain. By numbering the discrete points on all the boundaries globally in the sequence shown in Figure 2(a) (broken lines with arrows) and assembling a set of locally full coefficient matrices into a global matrix, the structure of this global matrix features block diagonalization (see Figure 2(b)). This band diagonal matrix is stored and manipulated in a so-called compact form, which results as if the matrix is tilted 45° clockwise. When efficiently structured, matrix diagonalization can lead to significant reductions in the requirement for reserved storage and in CPU time in both the generation of the coefficient matrix and the solution of the algebraic equations.

3.2. Optimization of domain decomposition

Matrix diagonalization is achieved at the price of an extended matrix; the net efficiency of this approach depends on both the topography of the domain and the way the domain is divided. In the case of a long wave tank the discretization of the free surface requires many more panels than exist on other boundaries (real or numerical). Therefore the wave tank topography is actually ideal for the implementation of the multi-subdomain approach. An appropriate domain discretization is to use vertical inner boundaries with an equal number of free surface grid points between them. The number of subdomains can be optimized to achieve the least computational time for the generation and solution of the algebraic equations.

It would be ideal to choose the minimum sum of T_{CM} (the time required to generate coefficient matrixes for algebraic equations) and T_{SE} (the time needed for solution of these equations) as the object of optimization. In BEM, T_{CM} is usually much larger than T_{SE}, so we first optimize T_{CM} here. As

shown earlier in Figure 2(a), m represents the number of panels on the water surface in each subdomain, n is the number of panels on the inner vertical boundary and the whole computational domain is divided into k subdomains. The total number of panels on the water surface is M and $m(k-1) < M \leq mk$, since M may not be exactly divisible by k. Thus, except that the number of nodes in the last subdomain may be equal to or less than $m + 2n + 1$, the number of nodes in each subdomain is constant and equal to $m + 2n + 1$. Then, with the multi-subdomain approach.

$$T_{CM} \sim k(m + 2n + 1)^2 = Mm + 2M(2n + 1) + \frac{M}{m}(2n + 1)^2 \tag{8}$$

and T_{CM} is minimized when

$$\frac{\partial T_{CM}}{\partial m} = M - \frac{M(2n + 1)^2}{m^2} = 0, \tag{9}$$

i.e.

$$m = 2n + 1; \tag{10}$$

this results in

$$T_{CM} \sim 4(2n + 1)M. \tag{11}$$

Equation (11) shows that the time for the formation of the coefficient matrix in the multi-subdomain approach is linearly proportional to the number of panels on the water surface rather than quadratically proportional as in the single-domain approach. The efficiency of the multi-subdomain approach can be partly seen in Figure 3(a), where the ratio of $(T_{CM})_M$ (multi-subdomain) over $(T_{CM})_S$ (single domain) is shown.

The time required to solve the equations, T_{SE}, can also be minimized in the same way and the optimized m is a solution of the third-degree equation

$$m^3 + pm + q = 0, \tag{12}$$

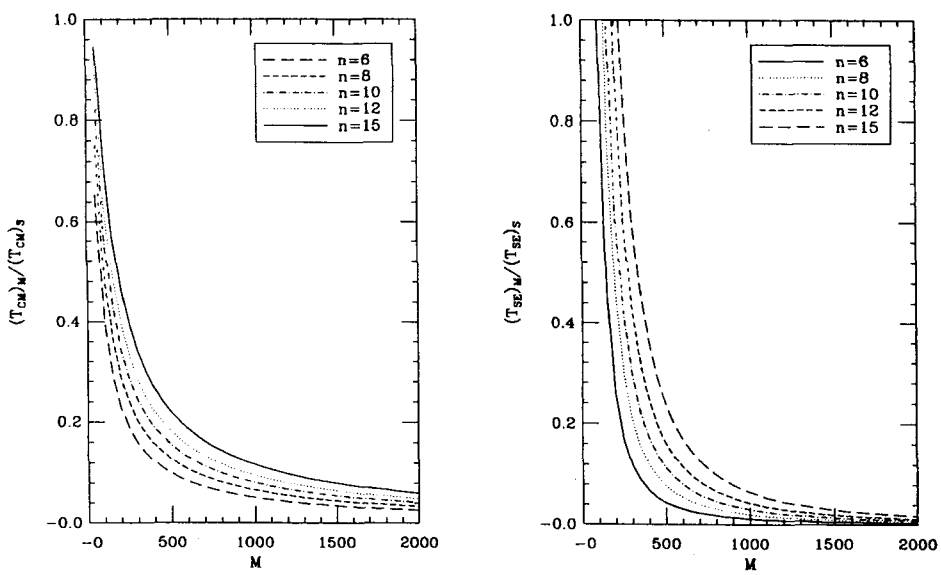

Figure 3. Efficiency of multi-subdomain approach compared with single-domain approach: (a) relative time for generating coefficient matrix; (b) relative time for solving linear algebraic equations

where

$$p = -\frac{(15n+1)M^2}{8n^2(6n+1)}, \qquad q = -\frac{3M^3}{8n^2(6n+1)}. \tag{13}$$

The optimal efficiency for solving equations can be seen in the ratio of $(T_{SE})_M$ (multi-subdomain) over $(T_{SE})_S$ (single domain) shown in Figure 3(b).

When the time for generation of coefficient matrixes is minimized, the time for solving equations is also decreased, even though it may not be minimized. The variation in efficiency with the number of panels on each subdomain is plotted in Figure 4 for a fixed panel number on vertical walls (n = 12) and for M = 1000, 2000, ..., 5000.

We conclude that the highest ensemble efficiency with the multi-subdomain approach is achieved when the number of panels on the free surface in each subdomain doubles the number on the vertical inner wall, equation (10). This high efficiency is clearly seen in Figure 5, showing a linear increase in CPU time with the panel number on the free surface.

Considering the short time involved in the final stage of breaking (less than half a wave period), the vertical inner boundaries are chosen so as to avoid them passing through the breaking region itself.

To demonstrate quantitatively the efficiency of MSD, the following example is given. For the case of 5000 nodes on the free surface and 10 nodes on each of the two ends, about 25·2 million (5020 × 5020) influence coefficients need to be calculated for set-up of 5020 equations in normal BEM, while only about 0·6 million (250 × 40 × 60) influence coefficients are needed for 10,000 equations in MSD with 249 vertical inner boundaries with 10 nodes on each of them. Thus MSD results in about 97·5% reduction in both storage and CPU time compared with normal BEM.

Figure 6 shows an example of *LONGTANK* simulation of strong wave grouping within a wave train of initial steepness of 0·14 generated by a wavemaker with 1% of the total wave energy in each of its resonant side-bands. This demonstrates the ability of *LONGTANK* for the study of the long-time evolution of water waves in space.

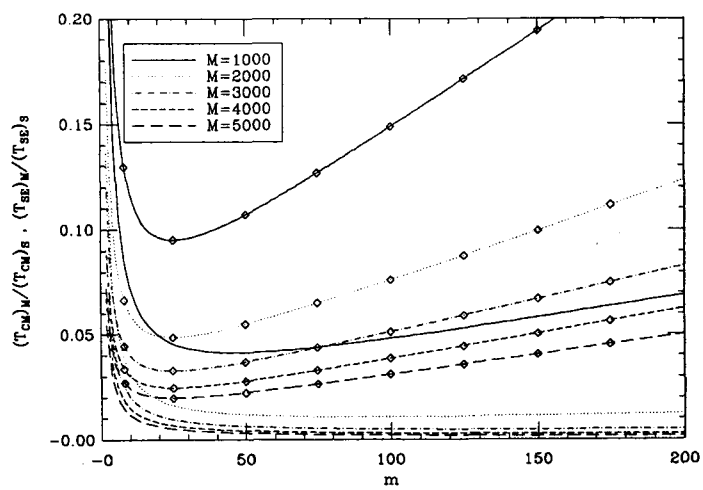

Figure 4. Ratio of time used with multi-subdomains over time used with single domain for generating coefficient matrix (with diamonds) and solving linear algebraic equations (no diamonds), versus panel number on free surface in each subdomain

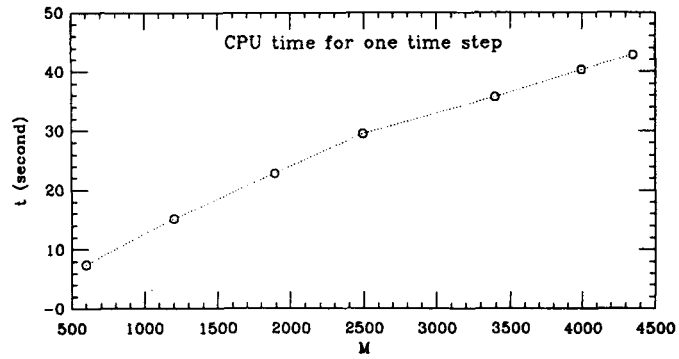

Figure 5. CPU per time step in wave calculation in *LONGTANK* versus number of panels on whole free surface

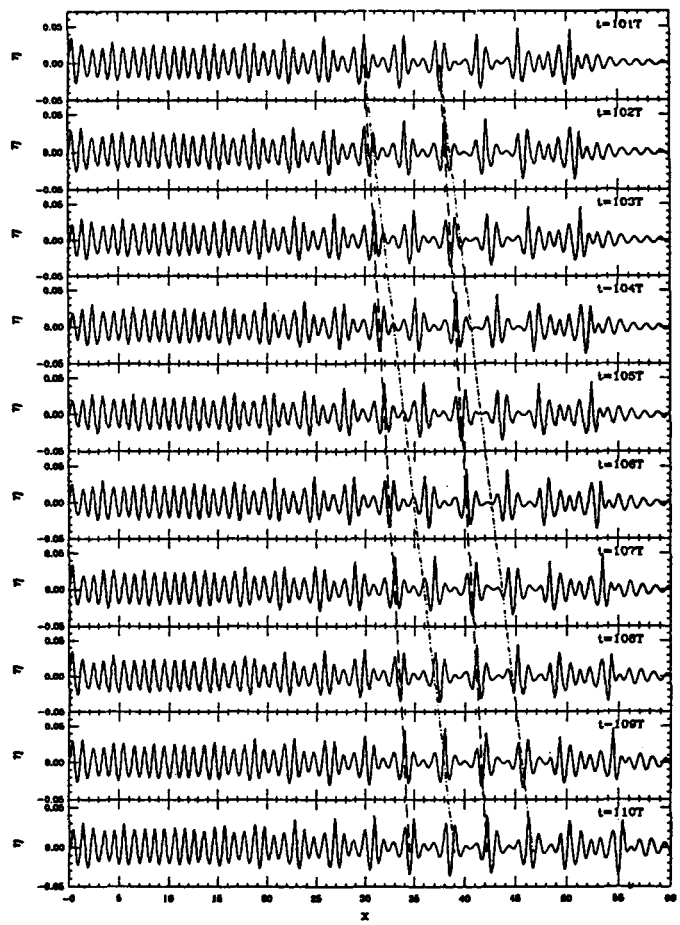

Figure 6. Simulated wave train (left to right), $a_0 k_0 = 0 \cdot 14$. Lines indicate propagation at group velocity (– –) and phase velocity (– · –). The front was suppressed and breaking did not occur

3.3. *Intersection of outer and inner boundaries*

In the interior of the computational domain the velocity potential and its derivatives are continuous but unknown prior to solution. When we insert vertical walls as shown in Figure 2(a), we introduce new unknowns on the inner boundaries in addition to those on the physical boundaries. At each point on these inner boundaries there are two unknowns, potential and normal velocity, and the equation must be set up twice, one in the subdomain on each side of the inner boundary. Thus the increased number of equations exactly matches the increased number of unknowns.

On the surface boundary the velocity potential is known from the previous time step using equations (3) and (4) and the tangential velocity can be obtained by Lagrangian interpolation; then the only unknown is the normal velocity. After discretization, one equation is set up at each discrete point which balances the single unknown there. Although at some surface points where an inner boundary is intersected two equations can be set up mathematically, the number of unknowns remains one; this fact could result in overdetermination. The detailed treatment will be given in Section 4.3.

4. *LONGTANK*—NUMERICAL IMPLEMENTATION

4.1. *Wave tank set-up and boundary discretization*

A two-dimensional numerical wave tank, *LONGTANK*, is set up with a wavemaker installed at the left end, which generates surface gravity waves that propagate along the tank a distance of up to 110 wavelengths. For shallow water cases a piston-type wavemaker (a vertical plate moving back and forth) is used; for deep water cases a plunger-type wavemaker (a wedge moving up and down) is employed. Other types of wavemakers can also be installed for specific purposes.

When the wavemaker begins to oscillate at the left end of the tank, waves begin to propagate on the originally still surface. In *LONGTANK* a movable end wall is set up initially at a distance of around five wavelengths to the right of the wavemaker. As the wavemaker oscillates, the end wall moves to the right and the tank is lengthened as needed.

To improve the efficiency of tank utilization and to avoid small waves reflecting back from the end wall, a numerical damping beach is attached to the moving end wall. The beach is capable of absorbing the longer waves that are of no interest to us but travel faster than the front of the wave train. The beach is always several wavelengths ahead of the main wave train and moves with the same speed as the wave

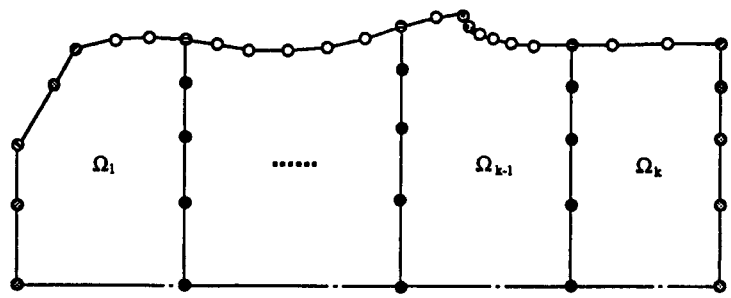

- Type 1 : Dirichlet condition, $\partial\phi/\partial n$ unknown
- Type 2 : Neumann condition, ϕ unknown
- Type 3 : Both ϕ and $\partial\phi/\partial n$ unknown
- Type 4 : $\partial\phi/\partial n$ known and discontinuous, ϕ unknown
- Type 5 : Intersection of the water surface with a moving body
- Type 6 : Dirichlet condition & high curvature
- Type 7 : Dirichlet condition & intersection point

Figure 7. Schematic of boundary discretization and grid types

train (group velocity), allowing effective use of the computational region while avoiding reflection from the end.

To solve the boundary integral equations numerically, the boundaries are discretized into linear elements (see Figure 7). Grid points on the water surface are fixed to water particles and equally spaced initially. Later they may be more concentrated on the wave crest and trough and less elsewhere. This natural tendency coincides with the numerical requirement that more grids are needed in regions of high curvature. On the vertical boundaries, including the front and end walls of the tank and numerical inner walls, the grid spacing is increased exponentially with depth because of the exponential decay of the velocity potential with depth. The boundary on the tank bottom can be removed by introducing tank images. Grids on all the boundaries are sorted into different types as indicated in Figure 7. The first three types are basic. Grids of type 4, where $\partial\phi/\partial n$ is known but discontinuous are easily handled by connecting $(\partial\phi/\partial n)^-$ to the left element and $(\partial\phi/\partial n)^+$ to the right element. Grids of types 5–7 need careful treatment which will be discussed in detail later.

4.2. *Integration and differentiation*

In *LONGTANK*, linear elements are chosen with both linear geometrical representation and interpolation, because all the integration in equation (7) can be expressed analytically and thus numerical integrations are avoided.

In a local co-ordinate system (ξ, η) with its origin at a field point, the ξ-axis in the tangential direction (clockwise) of the element and the η-axis normal to the element and pointing outwards we have

$$\int_\Gamma \phi \frac{\partial}{\partial n}(\ln r)\,\mathrm{d}\Gamma = \Sigma\left(\int_j^{j+1} \phi \frac{\partial}{\partial n}(\ln r)\,\mathrm{d}\Gamma\right) = \Sigma\left(\frac{\xi_{j+1}I_2 - I_4}{\xi_{j+1} - \xi_j}\phi_j + \frac{I_4 - \xi_j I_2}{\xi_{j+1} - \xi_j}\phi_{j+1}\right), \tag{14a}$$

$$\int_\Gamma \frac{\partial\phi}{\partial n}(\ln r)\,\mathrm{d}\Gamma = \Sigma\left(\int_j^{j+1} \frac{\partial\phi}{\partial n}(\ln r)\,\mathrm{d}\Gamma\right) = \Sigma\left[\frac{\xi_{j+1}I_1 - I_3}{\xi_{j+1} - \xi_j}\left(\frac{\partial\phi}{\partial n}\right)_j + \frac{I_3 - \xi_j I_1}{\xi_{j+1} - \xi_j}\left(\frac{\partial\phi}{\partial n}\right)_{j+1}\right], \tag{14b}$$

where I_1, I_2, I_3 and I_4 are integrations along elements of $\ln r, \partial n/\partial(\ln r)$, $\xi \ln r$ and $\xi\partial n/\partial(\ln r)$ respectively, all having a closed form.[16]

To project surface wave profiles from the current time onto the next time step, $\partial\phi/\partial s$ is also needed on the water surface. In general, differentiation based on three-point Lagrangian interpolation is applied in *LONGTANK*. Through numerical tests, generally 40 elements in one wavelength have been chosen.

During the last stage of wave breaking, a jet is formed from the wave crest, where higher and higher curvature evolves, so special treatment is needed near the tip of the jet which will be discussed in the following subsection.

4.3. *Treatments at special points on boundary*

Surface–wavemaker intersection. For wavemaking or wave–body interaction problems an appropriate treatment of the singularity at the intersection of the free surface with the body (grid of type 5 in Figure 7) is always required.

In *LONGTANK* the corner treatment is clearly shown in Figure 8(a). At the intersection point the potential itself is continuous but its tangential and normal derivatives are not because of geometric discontinuity. Assume that the superscripts '$-$' and '$+$' indicate respectively the left and right potential derivatives at that point. Excluding the extreme case of a jet forming at the intersection, we have the

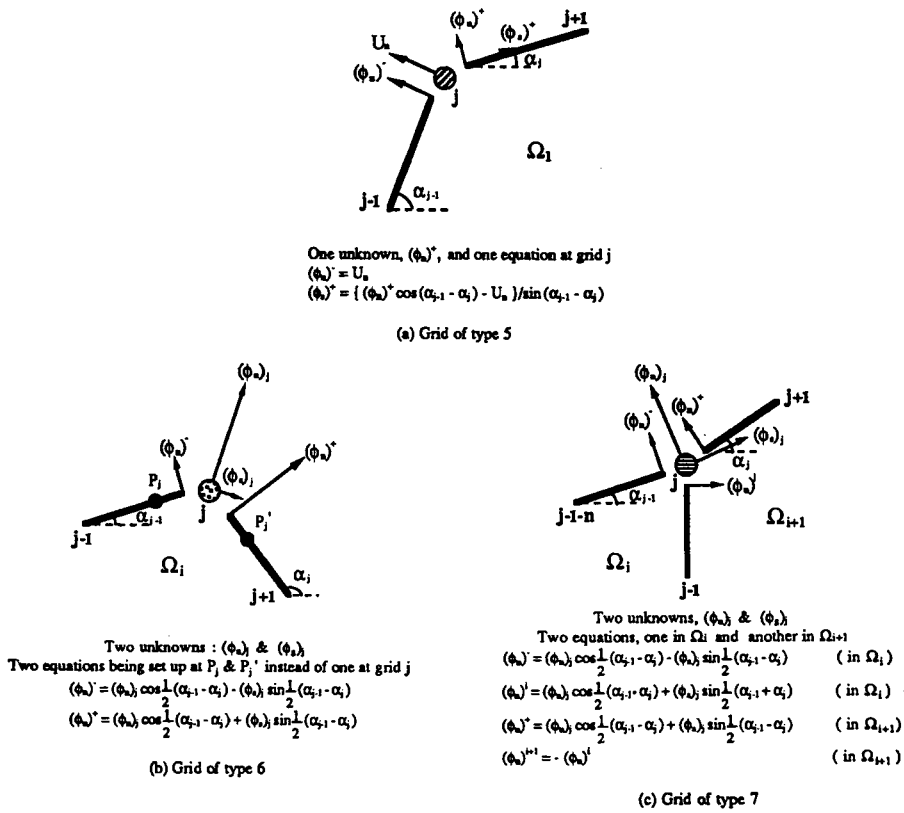

Figure 8. Treatments at special points on computational boundaries

two equations shown in Figure 8(a) which satisfy the kinematic condition on the boundary with the wavemaker. Because the motion of the wavemaker is imposed and its normal velocity U_n is only a function of time, there is only one independently unknown variable, $(\phi_n)^+$ or $(\phi_s)^+$. To be consistent with other surface points, we choose $(\phi_n)^+$ as the unknown variable, which can be solved from the boundary integral equation, and then $(\phi_s)^+$ can be determined from the kinematic condition given in Figure 8(a).

The treatment given here is more reliable and concise than that in References 5,17 and 18 and it is generally applicable to any wave-body intersection problem. Figure 9 shows an example of wave breaking near a wavemaker.

Surface point with high curvature. During the last stage of wave breaking, waves experience strong deformations: greater steepness, front face steepening and a jet forming at the crest. Then numerical differentiation will not be appropriate for the tangential derivatives of the velocity potential at those surface points where high curvature occurs owing to wave deformation (grids of type 6 in Figure 7). An alternative is to solve for them directly from the boundary integral equation together with normal derivatives at those points. Thus two equations at each grid of type 6 need to be established to balance the two unknown variables there. Song and Maruo[19] employed discontinuous elements introduced by Brebbia and Dominguez[20] to deal with the discontinuous normal derivatives at the tip of the spray and used extrapolation to get the two normal velocities at the tip. In *LONGTANK* (see Figure 8(b)) the two

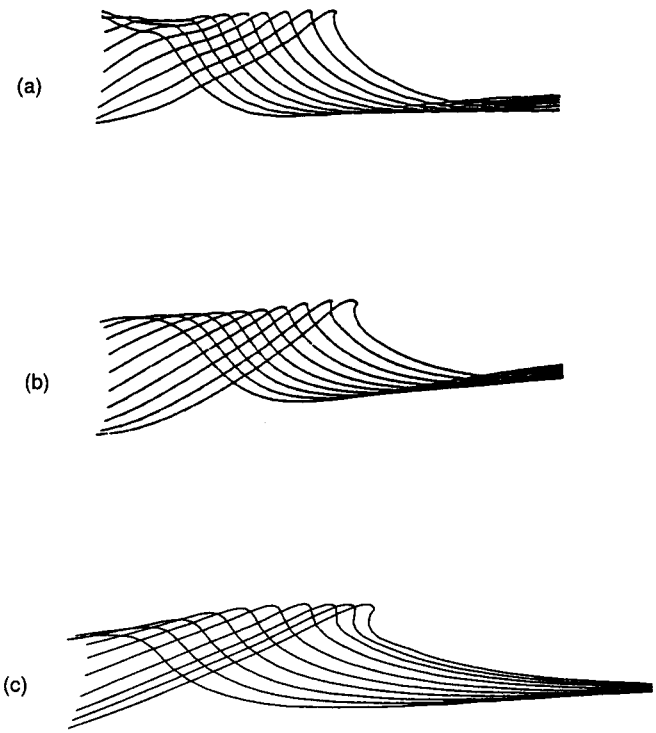

Figure 9. Wave breaking near wavemaker: (a) from Reference 5; (b) from Reference 17; (c) from *LONGTANK* simulation

unknown variables are the normal and tangential velocities at the central grid j. Two field points P_j and P'_j where equations are to be set up are put on two neighbouring elements near the central grid j and the

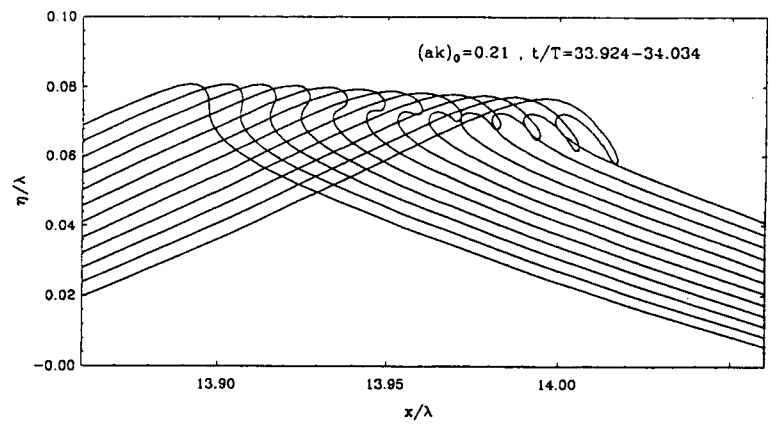

Figure 10. Wave breaking in *LONGTANK*, showing formation of a plunging jet

integrations on these two elements in the equations set up at P_j and P'_j can also be expressed analytically. No extrapolation is involved. The positions of P_j and P'_j on the neighbouring elements are fairly flexible except for the midpoint, which should be excluded in the case of two neighbouring grids both of type 6. In *LONGTANK* a distance to the central point j of 20% of the element length is chosen.

The breaking jets from numerical simulations in *LONGTANK* have smooth jet forms as shown in the experimental photograph of Bonmarin,[21] while all previous computational results in the literature show very sharp tips in the breaking jets which prevented the continuation of the computation. The detailed analysis of particle motion near the tip of the jet will further verify this numerical scheme.

Figure 10 shows an example of breaker formation within a strongly modulated wave train which has initial steepness 0·21.

Intersection of free surface with inner vertical boundary. In contrast with the surface point of high curvature, there are two possible equations at the intersection of the free surface with the inner vertical boundary. These two equations can be set up in subdomains on each side of the inner vertical boundary, while only one unknown variable exists (inner vertical boundaries are avoided in regions of high surface curvature). Possible treatments of this problem are: establishing an equation only once in either of two neighbouring subdomains; establishing two equations, one in a subdomain on each side, and introducing a tangential velocity at the intersection point into the unknown variable system which is actually not an independent unknown variable. Both these treatments achieve a balance between the numbers of unknowns and equations.

Our numerical tests found that with the former treatment the solved normal velocities have a little roughness near the intersection point, while with the latter treatment the solved normal velocities are smooth everywhere and the solved tangential velocities at the intersection points agree very well with those from numerical differentiation based on three-point Lagrangian interpolation along the free surface. The latter treatment is thus adopted in all *LONGTANK* simulations. Details are shown in Figure 8(c).

4.4. Jet refining and smoothing

According to convergence tests carried out in time and space, generally 40 nodes per wavelength on the free surface and 40 time steps in one wave period have been chosen. However, during the last stage of wave breaking, the wave first deforms, then steepens and finally a jet forms from the crest, where high curvatures occur and particles speed up rapidly. To capture the jet as precisely as possible, which is of importance in post-breaking studies, the time steps and the local grid number both need to be increased.

It is found that regridding slows down the process of jet forming artificially because it always suppresses the small jets that have just formed. It is appropriate to increase the density of the grid distribution in that small region by inserting new grids between the existing grids; we call this refining. Thus no information is lost and no accuracy is lost within the approximation of linear geometry and interpolation along the element.

In *LONGTANK* the refining begins with steepening of the front and the jet-forming process is closely monitored by temporarily halting the calculation and restarting again. The increase in grid number is gradual and restricted to a specified region; the time steps have to match the smallest grid space, since the velocity is accelerated during this time.

When the jet has well formed, a weak instability is sometimes found on the lower face of the jet. Local smoothing is thus applied when necessary. The uniform five-point smoothing formula used by Longuet-Higgins and Cokelet[4] is expanded here to general five-point smoothing.

Assume that the five points are $j-2$, $j-1$, j, $j+1$ and $j+2$. Move the origin of the curvilinear co-ordinates s onto the central point j and more generally let

$$\Delta s_1 = s_{j+1} - s_j, \qquad \Delta s_2 = s_{j+2} - s_j, \qquad \Delta s_{-1} = s_j - s_{j-1}, \qquad \Delta s_{-2} = s_j - s_{j-2}.$$

Then

$$\bar{f}_j = a_0 = \frac{-2\Delta s_{-1}(A_1 - A_2 + A_3) - 2\Delta s_1(A_4 - A_5 + A_6)}{4(\Delta s_{-1} + \Delta s_1)A_7}, \tag{15}$$

where

$$\begin{aligned}
A_1 &= (f_{j-2} - f_j)[(\Delta s_1)^2 \Delta s_2 + (\Delta s_2)^2 \Delta s_1],\\
A_2 &= (f_{j+1} + f_j)[(\Delta s_{-2})^2 \Delta s_2 + (\Delta s_2)^2 \Delta s_{-2}],\\
A_3 &= (f_{j+2} - f_j)[(\Delta s_1)^2 \Delta s_{-2} - (\Delta s_{-2})^2 \Delta s_1],\\
A_4 &= (f_{j-2} - f_j)[(\Delta s_{-1})^2 \Delta s_2 - (\Delta s_2)^2 \Delta s_{-1}],\\
A_5 &= (f_{j-1} + f_j)[(\Delta s_{-2})^2 \Delta s_2 + (\Delta s_2)^2 \Delta s_{-2}],\\
A_6 &= (f_{j+2} - f_j)[(\Delta s_{-2})^2 \Delta s_{-1} + (\Delta s_{-1})^2 \Delta s_{-2}],\\
A_7 &= (\Delta s_{-2})^2 \Delta s_2 + (\Delta s_2)^2 \Delta s_{-2}.
\end{aligned}$$

In the case of equal spacing, equation (15) gives exactly the uniform five-point smoothing formula used by Longuet-Higgins and Cokelet.[4].

Figure 11 shows an example of refining during breaking.

4.5. *Moving beach*

The idea of a numerical beach in a wave tank was earlier implemented by Baker *et al.*[10] Recently Cointe[8] applied this numerical beach to his own tank, which has a fixed tank length of about 10 wavelengths, and satisfactory absorption was achieved.

Physically it is the oscillations within the waves (including the position and potential of the water particles) that must be damped. Thus damping terms are added to the RHS of equations (3) and (4):

$$\frac{Dx}{Dt} = \frac{\partial \phi}{\partial x} - \gamma(x_e)(x - x_e), \tag{16}$$

$$\frac{Dy}{Dt} = \frac{\partial \phi}{\partial y} - \gamma(x_e)(y - y_e), \tag{17}$$

$$\frac{D\phi}{Dt} = -gy + \tfrac{1}{2}(\nabla\phi)^2 - \gamma(x_e)(\phi - \phi_e), \tag{18}$$

where $\gamma(x_e)$ is a damping coefficient and the subscript 'e' denotes the equilibrium state when there is no wave propagating.

As for the real tank, the beaches are designed to attenuate waves gradually over a certain distance L_b. In *LONGTANK*, in the damping region $x_b(t) \le x \le x_{END} = x_b(t) + L_b$, the damping coefficient is

taken in a form which is equivalent to that used by Baker *et al.*[10] and Cointe:[8]

$$\gamma(x_e) = \vartheta_b \left(\frac{x - x_b(t)}{L_b} \right)^2. \tag{19}$$

A quadratic increase in the damping intensity is chosen; ϑ_b is the magnitude of the damping intensity and has the unit of angular frequency. The choice of ϑ_b is crucial for successful absorption, so a more careful treatment than that of Cointe[8] is used here.

With insight given by equations (16)–(19), it is clear than ϑ_b can be simply chosen to be the wave frequency ω if the wave is monochromic and that the choice of ϑ_b is independent of L_b but depends on the magnitude (denoted by 'hats' in the following equations) of the oscillations divided by the

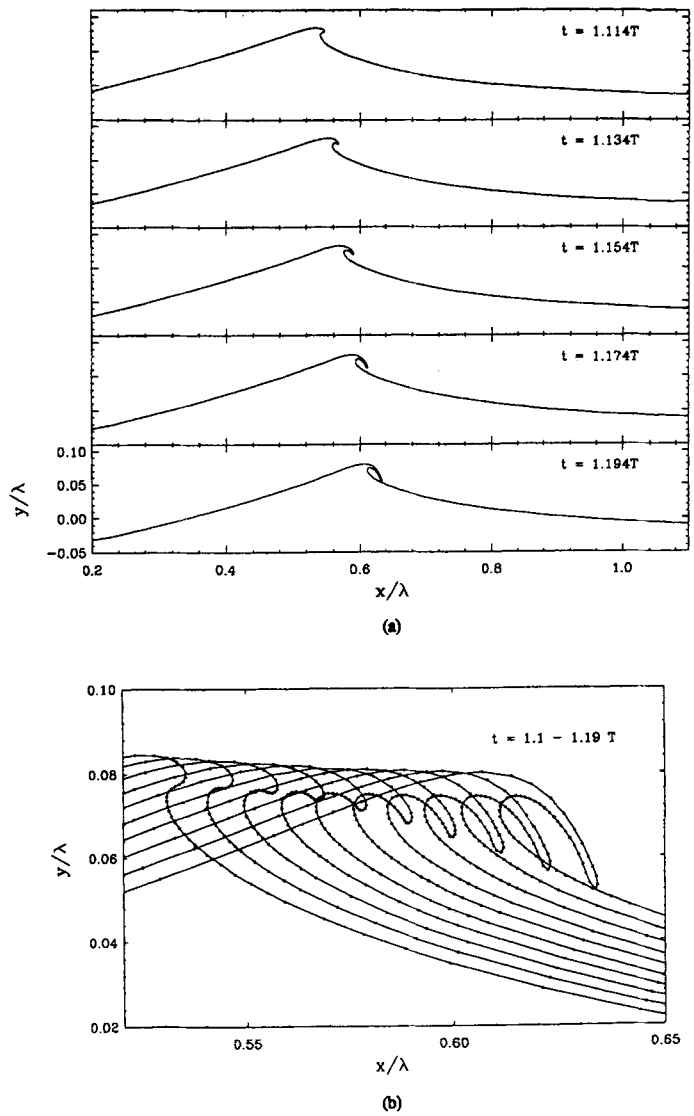

Figure 11. Wave breaking in *LONGTANK*, $a_0 k_0 \approx 0 \cdot 28$: (a) wave-forms in final stage of breaking: (b) formation of a plunging jet, showing refining technique

magnitude of the variable:

$$(\vartheta_b)_x = \widehat{\frac{\partial\phi}{\partial x}} \frac{2}{x_{\max} - x_{\min}}, \tag{20a}$$

$$(\vartheta_b)_y = \widehat{\frac{\partial\phi}{\partial y}} \frac{2}{y_{\max} - xy_{\min}}, \tag{20b}$$

$$(\vartheta_b)_\phi = \left(-g\frac{y_{\max} - y_{\min}}{2} + \tfrac{1}{2}(\widehat{\nabla\phi})^2\right) \frac{2}{\phi_{\max} - \phi_{\min}}, \tag{20c}$$

where all the variables are following particles as in a Lagrangian system.

The length of the beach determines how gently the waves are attenuated within the beach: the longer the beach is, the smaller are the dynamic effects left in the tank. In most cases a one-wavelength beach is appropriate.

Figure 12 presents a comparison of generated sinusoidal wave trains between *LONGTANK* simulations and corrected frequency domain solutions of Yao,[22] showing the efficiency of the moving beach in *LONGTANK*.

4.6. *'Peeling' technique*

Another numerical technique used in *LONGTANK* is 'peeling' of the top water of the wave crest to suppress undesirable breaking. It is observed in wave tank experiments that the leading crest in the wave train with a sufficient initial steepness usually breaks before the following crests, which will stop numerical computation. Thus it is desirable to suppress the breaking that occurs at the wave front in order to achieve breaking away from its influence. It is also desirable to suppress the breaking of waves prone to break within the train in order to allow successive breaking in the wave train. Therefore the

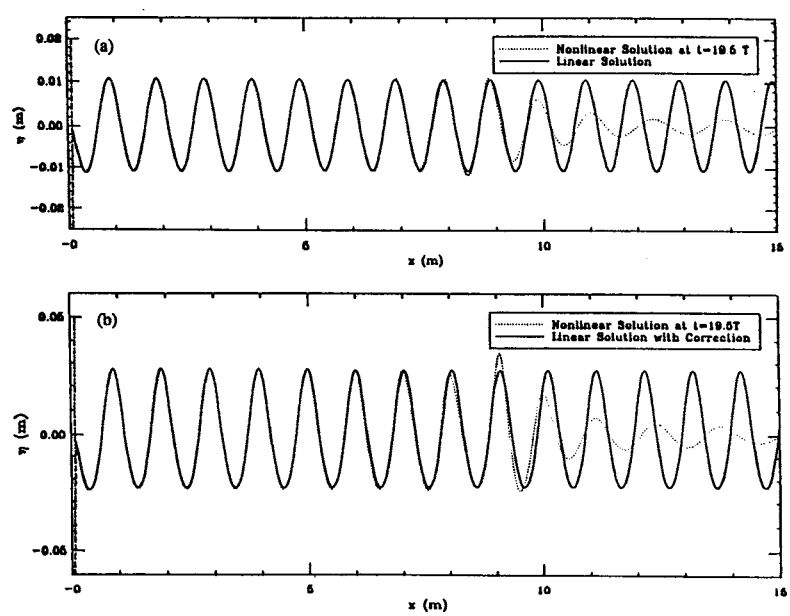

Figure 12. Comparison of sinusoidal wave trains between *LONGTANK* simulations and corrected linear solutions of Yao,[22] showing efficiency of moving beach in *LONGTANK*: (a) $a_0k_0 = 0 \cdot 07$; (b) $a_0k_0 = 0 \cdot 163$

technique called 'peeling' is developed for the mathematical suppression of breaking with minimum long-range effect.

The technique involves slowly 'peeling' away the water on the suppressed wave crest. A limiting wave height η_{LIMITING} is set for the wave crest under control. Determination of η_{LIMITING} is empirical in the current stage and η_{LIMITING} varies from $0 \cdot 25$ to $0 \cdot 28$ in *LONGTANK* suppressions depending on the initial wave steepness. As soon as the controlled crest climbs above this limiting height, i.e. $\eta_c > \eta_{\text{LIMITING}}$, a new free surface between two zero crossings is formed, $\eta' = \eta \times \eta_{\text{LIMITING}}/\eta_c$, by peeling away the top water to a relative maximum thickness $t_{\max} = (\eta_c - \eta_{\text{LIMITING}})/\eta_c$. As long as the time step is small (40 steps per period in *LONGTANK*) compared with the growth time of the crest, the thickness of the water layer being peeled away is very small ($t_{\max}$ is less than 3% in all our suppressions), so its static pressure can be neglected. The dynamic effect of the suppression is also small because of the slowness of 'peeling'. The potential on the new surface is predicted by exponential decay.

This technique has been applied at the front of wave trains as well as inside non-linear wave groups generated in *LONGTANK* for the study of wave breaking within groups. The insignificant long-range effect of suppression on the following waves is shown in Figure 13, where the leading wave is both suppressed and not.

4.7. Forward time stepping

Hammings' fourth-order predictor/corrector method has been applied for normal forward time stepping, while the fourth-order Runge–Kutta method has been used for forward time stepping at the beginning of the calculation or when new nodes are introduced on the free surface. The nodes on the free surface represent the water particles and move in the direction of the velocity vector. No numerical instability appears except occasionally on the lower face of the breaker.

4.8. Jet closure and splash

With the formation of a jet and its successive free fall, the jet impacts and penetrates the front face of the wave crest. In the conventional BEM formulation, even just before the initial impact, an ill-conditioned or nearly singular coefficient matrix will halt the BEM calculations. Thus a finite distance (not too small) between the jet and the front surface just before impact is required, otherwise they have to be treated as already touching. Furthermore, the modified single- and double-layer potential have to

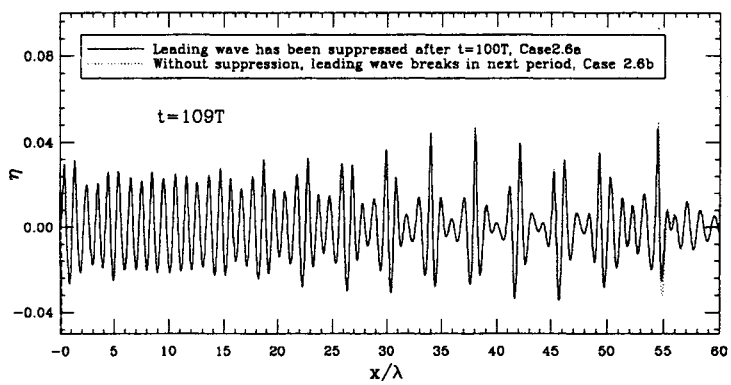

Figure 13. Simulated wave train, showing effect of front suppression

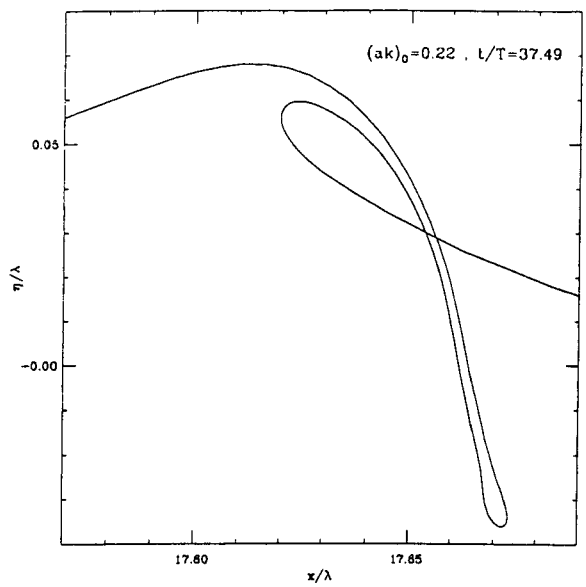

Figure 14. Plunging breaker computed as if the breaker does not see the surface. This demonstrates the continuation of breaking after impact

be applied on the common surface, as used by Zhang *et al.*[23] in the collapse of a cavitation bubble.

In the MSD approach, however, the penetration jet and impacted (or soon to be impacted) water surface can be easily arranged in different subdomains, thus avoiding the singular behaviour of close surfaces due to the BEM formulation. No modification of the boundary integral equation, applied in each subdomain, is required. Even without further specifying the physical impact conditions on the common surface, the computation can be continued as if the jet does not see the free surface (see Figure 14).

The initial stage of jet closure and splash can be simulated when appropriate physical conditions are applied on the common impact surface, which we discuss below.

Condition at instant of impact. As pointed by Zhang *et al.*[23] in the problem of bubble collapse, each node impact generates a pressure impulse I which is defined by

$$I = \lim_{t'' \to t'} \int_{t'}^{t''} P \, \mathrm{d}t, \tag{21}$$

where P is the impact pressure and t' and t'' represent the instants just before and after impact respectively. For infinitesimal time intervals from t' to t'' the relation between the velocity potentials ϕ' and ϕ'' just before and after impact respectively can be obtained from Bernoulli's equation:[24]

$$\phi'' - \phi' = -\frac{I}{\rho}. \tag{22}$$

Applying relation (22) to both impacting material points ('+' denotes the jet surface and '−' the front free surface) and noticing that the pressure impulses I^+ and I^- are equal, the condition at the instant of impact is obtained as

$$\phi''^{+} - \phi''^{-} = \phi'^{+} - \phi'^{-}, \tag{23}$$

which states that the difference in ϕ between two impacting points remains the same during the impact.[23]

Boundary conditions on the common surface. The kinematic boundary condition on the common surface after impact is that the velocity normal to the common surface is continuous across the interface:

$$\frac{\partial \phi^+}{\partial n^+} = -\frac{\partial \phi^-}{\partial n^-}, \tag{24}$$

where n^+ and n^- are outward normals to the upper (jet) and lower (front free surface) interfaces respectively.

The dynamic boundary condition is the continuity of the pressure across the interface:

$$P^+ = P^-. \tag{25}$$

Bernoulli's equation can be applied on both the upper and lower interfaces of the common surface:

$$\frac{\mathrm{D}\phi^\pm}{\mathrm{D}t} = \frac{1}{2}\left[\left(\frac{\partial \phi^\pm}{\partial n^\pm}\right)^2 + \left(\frac{\partial \phi^\pm}{\partial s}\right)^2\right] + \frac{P_\infty - P^\pm}{\rho}. \tag{26}$$

Using equations (24) and (25), the condition on the common interface is obtained as

$$\frac{\mathrm{D}\phi^+}{\mathrm{D}t} - \frac{\mathrm{D}\phi^-}{\mathrm{D}t} = \frac{1}{2}\left[\left(\frac{\partial \phi^+}{\partial s}\right)^2 - \left(\frac{\partial \phi^-}{\partial s}\right)^2\right]. \tag{27}$$

Realizing that the tangential velocity across the interface is discontinuous and that initially contacting fluid particles at the interface might move away from each other, the two material derivatives on the LHS of (27) have to follow two different particles. Time marching of equation (27) gives $\phi^+ - \phi^-$ at the next time instant for all pairs of previously contacting points. Then $\phi^+ - \phi^-$ for newly contacting points can be expressed after interpolation and will serve as one boundary condition. The other boundary condition is equation (24).

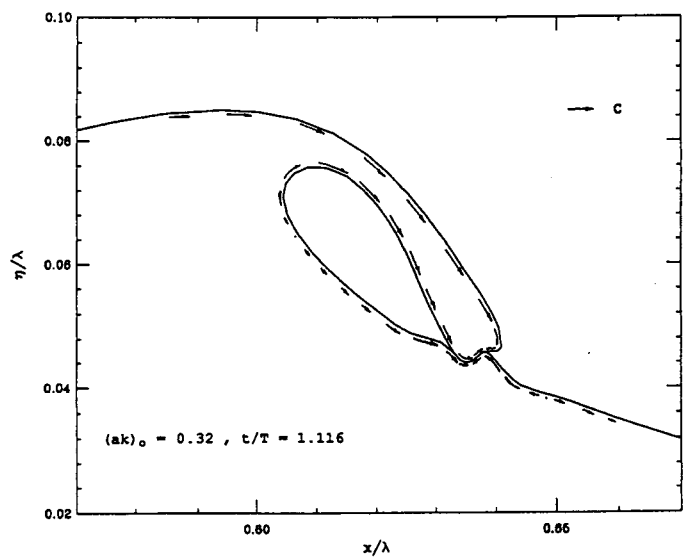

Figure 15. Initial stage of jet closure and splash. The tangential velocity around the jet is indicated

Figure 15 shows a preliminary simulation of the initial stage of jet closure and splash which is similar to the experimental observations of Tallent *et al.*[25] The tangential velocity, along the boundary of the new cavity and the common interface near the tip of the jet, has been indicated and the generated vorticity has been estimated.[12]

5. CONCLUSIONS

The multi-subdomain approach combined with the boundary element method has greatly enhanced the efficiency of computations in the 2D non-linear numerical wave tank. Featuring optimized matrix diagonalization when the number of surface nodes in each subdomain is double the number on the vertical inner boundary, this approach almost minimizes the computing time for both establishing and solving the boundary integral equations. This results in only a linear increase in CPU time with the total number of surface nodes in *LONGTANK* simulations.

The intersection points of the free surface with the vertical inner boundary have been appropriately treated by introducing the surface tangential velocity as the second unknown variable at those points and establishing an equation twice there, one in a subdomain on each side of the inner boundary. The numerical difficulty at the intersection of the free surface with the wavemaker, due to the discontinuity of normal velocity there, has been overcome using a correction procedure. The tangential velocity at surface points with high curvature has been calculated from the boundary integral equations instead of using a three-point Lagrangian interpolation of surface potentials.

The multi-subdomain approach together with a moving damping beach makes it possible for *LONGTANK* to simulate long-time evolutions of non-linear wave systems over sufficiently long distances, $x/\lambda = O(10^2)$. *LONGTANK* has been used to study non-linear processes in deep water waves of moderate steepness,[11] wave breaking in both shallow and deep water, breaker morphology, extreme wave and crest heights, breaking dissipation and vorticity generation,[12] the breaking criterion, long–short–wave interaction and breaking[13] with profitable results and findings.

With growth in side-bands, very strong modulations leading to group formation, accompanied by a strong modulation of energy distribution in space and wave deformation, are observed. The energy and energy density in each wave quadrant have been calculated through numerical integration of the total wave energy in each vertical column under its appropriate wave quadrant, determined by the zero crossing and position of crests and troughs. A concentration of wave energy in the centre of the group, especially in the central crest, is found and the energy density on the breaking (forward) quadrant exceeds levels elsewhere in the wave train.

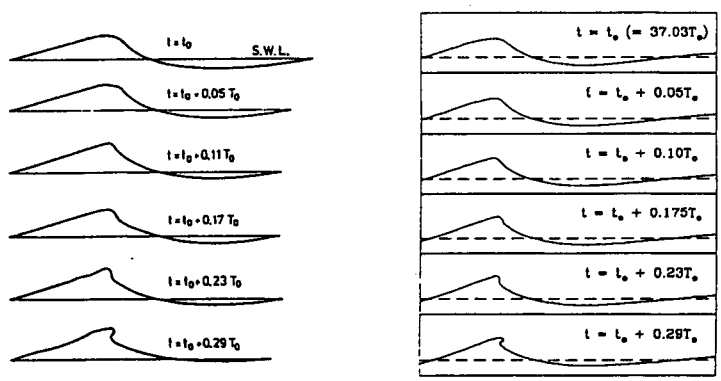

Figure 16. Wave-forms near breaking: (a) from Reference 26, $(ak)_0 \approx 0 \cdot 25$; (b) from *LONGTANK* simulations, $(ak)_0 = 0 \cdot 22$, case 2.1a

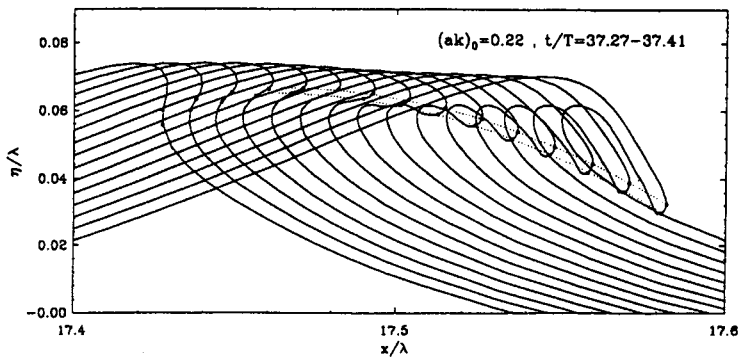

Figure 17. Evolution of a plunging jet following Figure 16 and preceding Figure 14: · · · · ·, ballistic particle trajectories (estimated); •, actual particle positions

Monitoring the horizontal particle velocity at the wave crest reveals a common phenomenon occurring in all *LONGTANK* simulations, suggesting a criterion for the inception of wave breaking: when and only when the horizontal particle velocity reaches $d\omega/dk$, wave breaking occurs inevitably in a short time, usually within a quarter of a wave period.[13]

Comparison of the time intervals and the corresponding wave-forms in the last stage of breaking between *LONGTANK* simulations and experimental photographs of Bonmarin and Ramamonjiarisoa[26] shows excellent agreement (see Figure 16). The steepness of the simulated waves at breaking and the downtank distance to breaking compare very favourably with measurements of Su and Green[9] (see Figure 16 of Reference 13 and Figure 6 of Reference 11). The local particle motion has also been studied in the simulations, showing that the particles near the tip of the jet almost exactly follow ballistic trajectories (see Figure 17), as expected since the pressure throughout the falling jet must be very close to atmospheric, leaving gravity as the dominant influence. These all tend to confirm the accuracy of *LONGTANK* simulation throughout the breaking stage.

ACKNOWLEDGEMENT

The authors are grateful for support from the Office of Naval Research, Ocean Technology Program, directed by Dr. Thomas Swean. We are also grateful to the CCSE (Prof. Stefan Boeriu) at UCSB and the San Diego Supercomputer Center for allocation of supercomputer access, which was highly important to us.

REFERENCES

1. M. P. Tulin and J. J. Li, 'On the breaking of energetic waves', *Int. J. Offshore Polar Eng.* **2**, 46–53 (1992)
2. J. W. Dold and D. H. Peregrine, 'Water-wave modulation', *Proc. 20th Int. Conf. on Coastal Engineering*, Taipei, 1986, pp. 163–175.
3. T. Vinje and P. Brevig, 'Numerical simulation of breaking waves, *Adv. Water Resources*, **4**, 77–82 (1981).
4. M. S. Longuet-Higgins and E. D. Cokelet, 'The deformation of steep surface waves on water. I. A numerical method of computation', *Proc. R. Soc. Lond. A*, **350**, 1–26 (1976).
5. W. M. Lin, J. N. Newman and D. K. P. Yue, 'Nonlinear forced motions of floating bodies', *Proc. 15th Symp. on Naval Hydrodynamics*, Hamburg, 1984, pp. 33–49.
6. D. G. Dommermuth, D. P. Yue, W. M. Lin, R. J. Rapp, E. S. Chan and W. K. Melville, 'Deep-water plunging breakers: a comparison between potential theory and experiments', *J. Fluid Mech.*, **189**, 423–442 (1988).
7. S. T. Grilli, J. Skourup and I. A. Svendsen, 'An efficient boundary element method for nonlinear water waves', *Eng. Anal. Bound. Elem.* **6**, 97–107 (1989).
8. R. Cointe, 'Numerical simulation of a wave channel', *Eng. Anal. Bound. Elem.* **7**, 167–177 (1990).

9. M. Y. Su and A. W. Green, 'Wave breaking and nonlinear instability coupling', in Y. Toba and H. Mitsuyas (eds), *The Ocean Surface*, 1985, pp. 31–38.
10. G. R. Baker, D. I. Meiron and S. A. Orszag, 'Generized vortex method for free-surface flow problems', *J. Fluid Mech.*, **123**, 477–501 (1981).
11. P. Wang, Y. Yao and M. P. Tulin, 'Wave group evolution, wave deformation, and breaking: simulation using LONGTANK, a numerical wave tank', *Int. J. Offshore Polar Eng.*, **4**, 200–205 (1994).
12. M. P. Tulin, Y. Yao and P. Wang, 'The simulation of the deformation and breaking of ocean waves in wave groups', *BOSS'94—7th Int. Conf. on Behaviour of Offshore Structures*, Elsevier, Amsterdam, 1994, pp. 383–392.
13. Y. Yao, P. Wang and M. P. Tulin, 'Wave groups, wave–wave interaction and wave breaking: results of numerical experiments', *Proc. 20th ONR Symp. on Naval Hydrodynamics*, Santa Barbara, CA, 1994, National Academy Press, in press.
14. W. M. Lin, 'Nonlinear motion of the free surface near a moving body', *Ph.D. Dissertation*, MIT, Cambridge, MA, 1984.
15. R. W. Yueng, 'Numerical methods in free surface flows', *Ann. Rev. Fluid Mech.*, **14**, 395–442 (1982).
16. J. A. Liggett, in D. E. Beskos (ed.), *Boundary Element Methods in Mechanics*, North-Holland, Amsterdam, 1987, Chap. 8.
17. R. Cointe, 'Remarks on the numerical treatment of the intersection point between a rigid body and a free surface', *Proc. Third Int. Workshop on Water Waves and Floating Bodies*, Woods Hole, MA, 1988.
18. S. T. Grilli and I. A. Svendsen, 'Corner problems and global accuracy in the boundary element solution of nonlinear wave flows', *Eng. Anal. Bound. Elem.* **7**, 178–195 (1990).
19. W. Song and H. Maruo, 'Bow impact and deck wetness: simulations based on nonlinear slender body theory', *Proc. Third Int. Offshore and Polar Engineering Conf.*, 1993, Vol. III, pp. 34–38.
20. C. A. Brebbia and J. Dominguez, *Boundary Elements, an Introductory Course*, McGraw-Hill, New York, 1989, pp. 70–74.
21. P. Bonmarin, 'Geometric properties of deep-water breaking waves', *J. Fluid Mech.*, **209**, 405–433 (1989).
22. Y. Yao, 'Theoretical and experimental studies of wavemaking by a large oscillating body in long tanks, including non-linear phenomena near resonance', *Ph.D. Dissertation*, University of California, Santa Barbara, CA, 1992, Sect. 10.2.
23. S. Zhang, J. Duncan and G. L. Chahine, 'The final stage of the collapse of a cavitation bubble near a rigid wall', *J. Fluid Mech.*, **257**, 147–181 (1993).
24. G. K. Batchelor, *An Introduction to Fluid Dynamics*, Cambridge University Press, Cambridge, 1967.
25. J. R. Tallent, T. Yamashita and Y. Tsuchiya, 'Transformation characteristics of breaking water waves', in A. Torum and O. T. Gudmestad (eds), *Water Wave Kinematics*, 1990, pp. 509–523.
26. P. Bonmarin and A. Ramamonjiarisoa, 'Deformation to breaking of deep water gravity waves', *Exp. Fluids*, **3**, 11–16.
27. B. M. Lake, H. C. Yuen, H. Rungaldier and W. E. Ferguson, 'Nonlinear deep-water waves: theory and experiment. Part 2. Evolution of a continuous wave train', *J. Fluid Mech.*, **83**, 49–74 (1977).
28. P. Wang, 'Numerical research on (I) ship internal waves and (II) breaking waves, *Ph.D. Dissertation*, University of California, Santa Barbara, CA, 1993.